

# The multiple coherence scales of C<sub>IV</sub> at cosmic noon

H. Cortés-Muñoz<sup>1</sup>, S. Lopez<sup>1</sup>, N. Tejos<sup>2</sup>, J.-K. Krogager<sup>3,4</sup>, D. Zamora<sup>1</sup>, R. Cuellar<sup>1</sup>, P. Anshul<sup>1</sup>, F. Urbina<sup>5</sup>, and A. Afruni<sup>6,7</sup>

<sup>1</sup> Departamento de Astronomía, Universidad de Chile, Casilla 36-D, Santiago, Chile. e-mail: hcortes@das.uchile.cl

<sup>2</sup> Instituto de Física, Pontificia Universidad Católica de Valparaíso, Casilla 4059 Valparaíso, Chile

<sup>3</sup> French-Chilean Laboratory for Astronomy, IRL 3386, CNRS and U. de Chile, Casilla 36-D, Santiago, Chile

<sup>4</sup> Centre de Recherche Astrophysique de Lyon, Université de Lyon 1, ENS-Lyon, UMR5574, 9 Av Charles André, 69230 Saint-Genis-Laval, France

<sup>5</sup> Kapteyn Astronomical Institute, University of Groningen, Landleven 12, 9747 AD Groningen, The Netherlands

<sup>6</sup> Dipartimento di Fisica e Astronomia, Università di Firenze, Via G. Sansone 1, 50019 Sesto Fiorentino, Firenze, Italy.

<sup>7</sup> INAF - Osservatorio Astrofisico di Arcetri, Largo E. Fermi 5, Firenze, I-50125, Italy.

November 15, 2025

## ABSTRACT

The spatial and kinematic structure of the circumgalactic medium (CGM) remains poorly constrained observationally. In this article we compute the clustering of C<sub>IV</sub> absorption systems at cosmic noon using quasar pairs. We analyze VLT/UVES and Keck/HIRES high-resolution spectra ( $R \sim 45\,000$ ) of a sample of 8 projected and 4 lensed quasar pairs that probe transverse separations,  $\Delta r$ , from sub-kpc to a few Mpc, over the redshift range  $1.6 \lesssim z \lesssim 3.3$ . We detect and fit Voigt profiles to a total of 141 C<sub>IV</sub> systems, corresponding to 620 velocity components across all quasar lines-of-sight. We compute the two-point correlation function of C<sub>IV</sub>,  $\xi(\Delta v, \Delta r)$ , where  $\Delta v$  is the velocity difference between components across all available scales. We find a strong dependence of  $\xi(\Delta r)$  with  $\Delta r$  at all velocities.  $\xi(\Delta r)$  reaches a sharp peak at the smallest scales analyzed here,  $\Delta r \approx 0.1$  kpc, decreases steadily up to  $\Delta r \approx 5$  kpc and remains flat up to  $\Delta r \approx 500$  kpc, where it begins to decrease again. By fitting power-laws to the projected transverse correlation function  $\Xi(\Delta r)$ , we infer two coherence lengths:  $r_1 = 654^{+100}_{-87}$  kpc, which we interpret as a representative size for the C<sub>IV</sub> enriched regions at  $z \approx 2$ , and  $r_2 = 4.70^{+1.60}_{-1.19}$  kpc for the individual C<sub>IV</sub>-bearing "clouds". Projecting instead in  $\Delta r$ , we find consistent amplitudes of  $\xi(\Delta v)$  with previous work using quasars and extended background sources. Our results suggest that C<sub>IV</sub> may be a good tracer of not only the small, internal structure of the circumgalactic medium, but also of the way in which galaxies cluster at cosmic noon.

**Key words.** cosmology: observations – quasars: absorption lines – galaxies: intergalactic medium

## 1. Introduction

The formation and evolution of galaxies is believed to leave an indelible mark on the spatial and kinematic structure of the circumgalactic medium (CGM; Tumlinson et al. 2017; Péroux & Howk 2020; Faucher-Giguère & Oh 2023). This is due to the baryon cycle, where gas flows in and out of galaxies through the CGM (Kereš et al. 2005; Oppenheimer & Davé 2006; Faucher-Giguère & Kereš 2011; Nelson et al. 2016). Since the CGM is diffuse, and usually too faint for direct observations, this gas is typically studied in absorption towards bright background sources, such as quasars (e.g., D’Odorico et al. 2010; Cooksey et al. 2013; Kim et al. 2013; Lehner et al. 2018; Churchill et al. 2020), galaxies (e.g., Steidel et al. 2010; Rubin et al. 2014; Bordoloi et al. 2017; Cooke & O’Meara 2015; Chen et al. 2020) and gamma-ray burst afterglows (e.g., Prochter et al. 2006; Tejos et al. 2007, 2009; Vergani et al. 2009; Bolmer et al. 2018; Saccardi et al. 2023; Krogager et al. 2024).

However, the use of single lines-of-sight prevents unambiguous determination of the gas spatial structure and clustering. An alternative is the use of the close, parallel lines-of-sight provided by multiple quasars in general (Hennawi et al. 2006; Coppolani et al. 2006; Martin et al. 2010; Tejos et al. 2014; Mintz et al. 2022; Urbano Stawinski et al. 2023), lensed

quasars (Rauch et al. 1999; Lopez et al. 1999, 2005, 2007; Chen et al. 2014; Zahedy et al. 2016; Krogager et al. 2018; Cristiani et al. 2024; Dutta et al. 2024), and lensed galaxies (Lopez et al. 2018, 2020; Mortensen et al. 2021; Tejos et al. 2021; Bordoloi et al. 2022; Fernandez-Figueroa et al. 2022; Afruni et al. 2023; Lopez et al. 2024). Remarkably, multiple lines-of-sight, although rare, considerably expand the information provided by single lines-of-sight, promising unique clues on the extent and coherence of the absorbers.

In this paper we concentrate on the spatial structure of C<sub>IV</sub> absorption systems, signposted through the C<sub>IV</sub>  $\lambda\lambda 1548, 1550$  doublet, an easy-to-find and representative tracer of the cool and warm CGM at  $z \gtrsim 1.5$  (e.g., Schaye et al. 2003; Songaila 2005; D’Odorico et al. 2010, 2013; Cooksey et al. 2013; Boksenberg & Sargent 2015; Hasan et al. 2020). Measurements using both transverse (e.g., D’Odorico et al. 2006; Martin et al. 2010; Maitra et al. 2019; Mintz et al. 2022) and line-of-sight (e.g., Scannapieco et al. 2006; Boksenberg & Sargent 2015; Welsh et al. 2025) correlations show that the clustering amplitude of strong C<sub>IV</sub> absorbers on Mpc scales is comparable to galaxy clustering. Since the C<sub>IV</sub>-galaxy cross-correlation is also significant (Adelberger et al. 2005; Banerjee et al. 2023), the picture that emerges is consistent with C<sub>IV</sub> arising predominantly in enriched gas associated with galaxy halos and their surrounding environments. However, these studies have fo-

cused mostly on larger scales, with very few studies venturing into small-scale clustering of the CGM (e.g., [Rauch et al. 2001](#); [Lopez et al. 2024](#)). Here we present the largest archival sample of echelle spectra of closely separated quasar pairs and use it to measure the C IV two-point autocorrelation function over transverse scales from the sub-kpc and up to a few Mpc. This allows us to estimate both the scale of the CGM and the sizes of individual clouds of C IV. Throughout this article, we assume a  $\Lambda$ CDM cosmology with parameters  $H_0 = 70 \text{ km s}^{-1} \text{ Mpc}^{-1}$ ,  $\Omega_m = 0.3$ , and  $\Omega_\Lambda = 0.7$ . Every distance measurement is comoving, unless stated otherwise.

## 2. Data

### 2.1. Sample construction

To build a statistically significant and as complete a sample as possible of quasar pairs with high resolution spectroscopy, we searched in the KODIAQ ([O'Meara et al. 2015, 2017](#)), and the SQUAD ([Murphy et al. 2019](#)) databases of Keck/HIRES and VLT/UVES spectra, respectively. We used the TOPCAT tool ([Taylor 2020](#)) to find suitable on-sky projected pairs. We limited the search to pairs with maximum transverse physical separations less than 1 Mpc (this translates to a couple of comoving Mpc at these redshifts; see Section 3.3) and emission redshifts  $z_{em} > 2$  to ensure coverage of C IV. The search delivered 9 quasar pairs, of which 1 is a lensed quasar (see Table 1). These spectra are both reduced and continuum normalized on their respective databases. We complemented the sample with additional high-resolution spectra of three lensed pairs found in the literature: J1029+2623 (PID: 092.B-0512(A)), HE 1104-1805, and RX J0911.4+0551 ([Lopez et al. 2005, 2007](#)). All archival spectra are reduced and normalized in a standard fashion. The exception is J1029+2623, for this case its reduced spectra were extracted from the archive and then combined to a common array by interpolating their wavelengths, averaging each flux pixel weighting by the inverse variance of each spectrum; while continuum normalization for this pair was carried out independently for both lines-of-sight by spline fitting using the LINETOOLS code ([Prochaska et al. 2016](#)). The final sample is made of the resolved echelle spectra of 4 lensed and 8 projected quasar pairs, summarized in Table 1. Emission redshifts lie in the range  $2.08 \leq z \leq 3.22$ . The resolving power is around  $R = \lambda/\Delta\lambda \approx 45\,000$  ( $\approx 6.6 \text{ km s}^{-1}$ ), and the typical wavelength range is  $3000 - 10000 \text{ \AA}$ , with variable coverage depending on the target. Signal-to-noise ratios (S/N) range between 5 and 100.

### 2.2. Redshift path

The S/N at a given wavelength on line-of-sight A (the brighter spectrum) and line-of-sight B (the fainter spectrum) are usually different. To evaluate these differences, we computed the redshift path density for C IV detection:

$$g(N_{min}, z) = \sum_{n=1}^{N_{LOS}} H(z - z_n^{min}) H(z_n^{max} - z) H(N_{min} - N_{lim}(z)), \quad (1)$$

where  $H$  is the Heaviside step function;  $z_n^{min}$  and  $z_n^{max}$  are redshifts ranges of line-of-sight number  $n$ , where we search for C IV between the Ly $\alpha$  and C IV emission lines of the quasar;  $N_{min}$  is the column density threshold; and  $N_{lim}$  is the minimum column density observable at redshift  $z$ .  $N_{lim}$  is computed at the  $3\sigma$  level

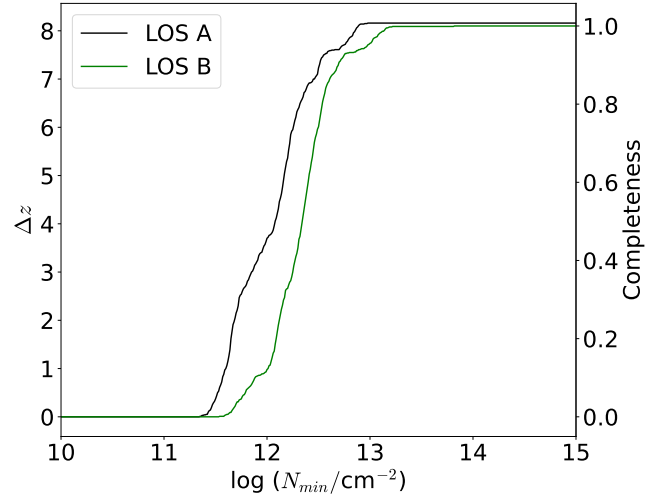


Fig. 1: Redshift path ( $\Delta z$ ) and completeness for line-of-sight A (B) in black (green) as a function of column density threshold ( $N_{min}$ ).

as ([Savage & Sembach 1991](#)):

$$N_{lim} = 1.13 \times 10^{20} \frac{W_{lim}}{\lambda_0^2 f} \text{ cm}^{-2}, \quad (2)$$

where  $f$  is the oscillator strength of the transition with wavelength  $\lambda_0 = 1548.2040$ , and  $W_{lim} = 3 \times \text{FWHM}/\langle S/N \rangle(1+z)$ . Here  $\langle S/N \rangle$  corresponds to the average signal-to-noise around redshift  $z$ , and  $\text{FWHM} = \lambda/R$ . Finally, by integrating  $g(N_{min}, z)$  over redshift, we obtained the redshift path,  $\Delta z = \int_{z_{min}}^{z_{max}} g(N_{min}, z) dz$ . Fig. 1 shows  $\Delta z(N_{min})$  for each line-of-sight. The  $\Delta z(N_{min})$  can be associated with a completeness level, by comparing with the total  $\Delta z$ . 90% completeness for C IV detection is reached at  $\log(N/\text{cm}^{-2}) = 12.51$  for lines-of-sight A, and  $\log(N/\text{cm}^{-2}) = 12.69$  for lines-of-sight B. This way, we find a total redshift path (as given by a  $N_{min}$  that gives 100% completeness) of  $\Delta z \approx 8.16$  on lines-of-sight A, and  $\Delta z \approx 8.1$  on lines-of-sight B. The small difference in  $\Delta z$  between lines-of-sight is due to minimal differences in wavelength coverage. We address this difference in  $\Delta z$  with the construction of random absorption catalogues to compute the two-point autocorrelation function in Section 4.1.

## 3. Absorption lines analysis

### 3.1. Absorption line identification and fitting

To identify C IV absorption systems, we automatically searched for peaks of optical depth in the wavelength range between Ly $\alpha$  and C IV emission lines, and selected by eye those compatible with both the doublet line separation, and doublet ratio. This approach identifies 73 systems for lines-of-sight A, and 68 for lines-of-sight B. To accurately measure the redshifts of the individual C IV velocity components on each absorption system, we fitted Voigt profiles to each system, using the VoigtFit Python package ([Krogager 2018](#)). Before fitting, we masked each region for bad pixels. In case interlopers overlapped with a C IV absorption system, they were fitted together. The fits were performed on each line-of-sight independently. On a first approach, we considered a fit successful when a VoigtFit model converged for

Table 1: Lensed and projected quasars pairs.

Type	$z_{\text{lens}}$	Quasar (A)	$z_{\text{quasar}}$ (A)	Quasar (B)	$z_{\text{quasar}}$ (B)	Separation (")	Reference
Lensed	0.490	Q0142-100 (A)	2.720	Q0142-100 (B)	2.720	2.24	(1)
Lensed	0.770	RX J0911.4+0551 (A)	2.800	RX J0911.4+0551 (B)	2.800	2.47	(2)
Lensed	0.550	J1029+2623 (A)	2.197	J1029+2623 (B)	2.197	22.50	(3)
Lensed	0.730	HE 1104-1805 (A)	2.320	HE 1104-1805 (B)	2.320	3.19	(2)
Projected		J000852-290043	2.645	J000857-290126	2.607	78.48	(4)
Projected		J030640-301031	2.096	J030643-301107	2.130	51.66	(4)
Projected		J031006-192124	2.122	J031009-192207	2.144	60.47	(4)
Projected		J143229-010614	2.087	J143229-010616	2.076	4.12	(4)
Projected		J214222-441929	3.230	J214225-442018	3.220	62.14	(4)
Projected		J223948-294748	2.121	J223951-294836	2.068	63.60	(4)
Projected		J234625+124743	2.515	J234628+124858	2.568	85.04	(4)
Projected		J234819+005717	2.163	J234819+005721	2.145	7.03	(4)

References. (1) O'Meara et al. (2015, 2017); (2) Lopez et al. (2005, 2007); (3) PID: 092.B-0512(A) (PI Saez); (4) Murphy et al. (2019)

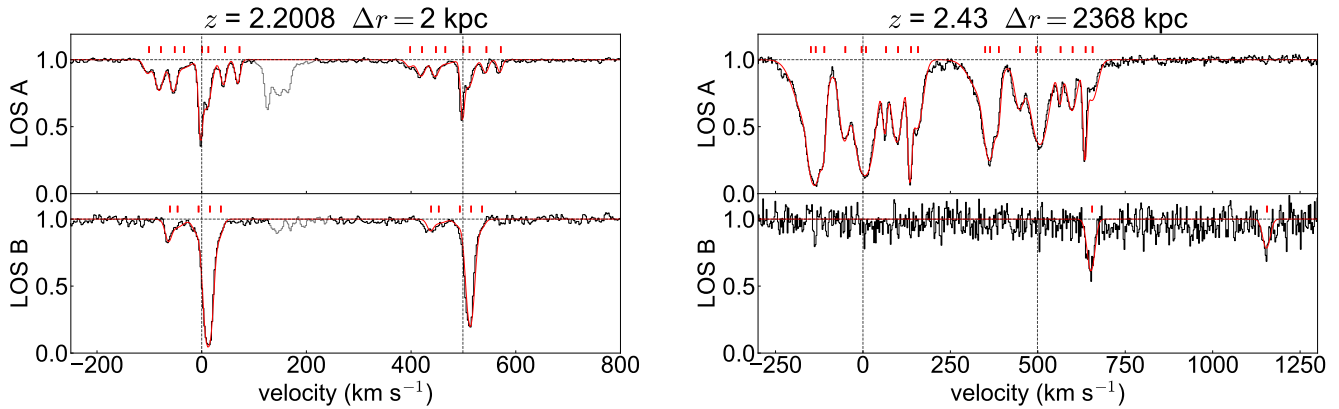


Fig. 2: Examples of C<sub>IV</sub> absorption systems fitted with Voigt profiles. Left panel: absorption system at  $z_{\text{abs}} = 2.2008$  towards the lensed quasar HE 1104-1805. Right panel: absorption system at  $z_{\text{abs}} = 2.43$  towards J234628+124858 and J234625+124743. Top (bottom) panels correspond to line-of-sight A (B). The black histogram corresponds to the normalized flux of the quasars, and the red lines correspond to the Voigt profile fit of the system. The velocity zero-point was chosen by eye around the 1548 Å C<sub>IV</sub> line.

the whole system. Moreover, we computed a component-by-component "badness parameter" (Churchill et al. 2020):

$$\text{badness} = \left[ \left( \frac{\sigma_N}{N} \right)^2 + \left( \frac{\sigma_b}{b} \right)^2 + \left( \frac{\sigma_z}{z} \right)^2 \right]^{1/2}, \quad (3)$$

where  $\sigma_N$ ,  $\sigma_b$ , and  $\sigma_z$ , are the uncertainties determined by VoigtFit for column density ( $N$ ), Doppler parameter ( $b$ ), and redshift ( $z$ ), respectively. Individual velocity components with badness  $> 1.5$  were re-fitted with different initial parameters. This robustness check helped us to find more physically motivated components, avoiding unreasonably large or small results for the fitted parameters without much intervention; however, the final accepted fits are still a human decision. Considering all pairs, we found 327 C<sub>IV</sub> velocity components in lines-of-sight A, and 293 in lines-of-sight B. The redshift range of this sample is  $1.51 < z < 3.23$ . Fig 2 shows two examples of absorption systems, along with their Voigt profile fits, at two extreme comoving transverse separations,  $\Delta r$ . Qualitatively, this comparison suggests that smaller  $\Delta r$  probes more coherent structures than larger  $\Delta r$ .

### 3.2. Column density distribution

Another way to assess the completeness of our sample is the column density distribution,  $f(N, z)$ . We calculated  $f(N, z)$  following Eqs. (6) and (7) of Zafar et al. (2013). In Fig. 3, we show  $f(N, z)$  independently for lines-of-sight A and B. This distribution can be fitted by a power law,  $f(N, z) = C \times N^{-\delta}$ , where  $C$  is a normalization constant and  $\delta$  is the slope of the power law; we obtained the best fit parameters  $\log(C) = 9.00 \pm 0.78$ , and  $\delta = 1.66 \pm 0.06$  for lines-of-sight A, while for lines-of-sight B we find  $\log(C) = 10.58 \pm 1.81$ , and  $\delta = 1.77 \pm 0.13$ . We limited these fits to  $N > 10^{13} \text{ cm}^{-2}$ , where both A and B have similar completeness levels. Our fits are in good agreement with previous results by Kim et al. (2013) at  $1.9 < z < 3.2$  ( $\delta = 1.85 \pm 0.13$ ), and D'Odorico et al. (2010) at  $1.6 < z < 3.6$  ( $\delta = 1.71 \pm 0.07$ ), using similar redshift path and instrumental resolution. We believe this agreement is a strong diagnostic for the completeness of the survey, and supports our confidence on the Voigt profile fitting.

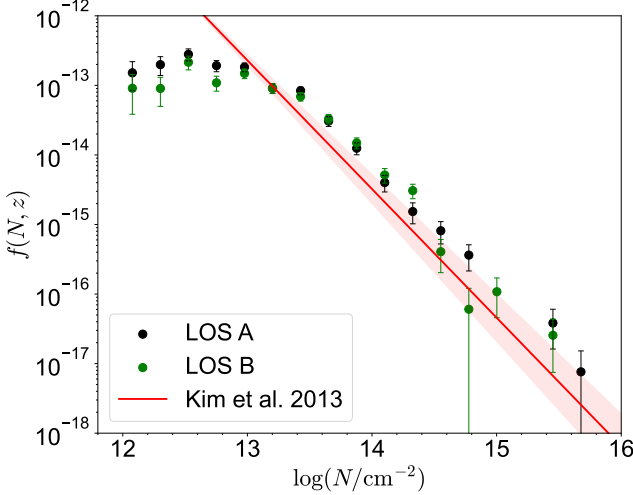


Fig. 3: CIV column density distribution for lines-of-sight A in black and lines-of-sight B in green. The pink solid line corresponds to the power law fit by [Kim et al. \(2013\)](#) to data of 18 VLT/UVES single quasar sightlines, while the shaded area is the  $1\sigma$  uncertainty in the fit.

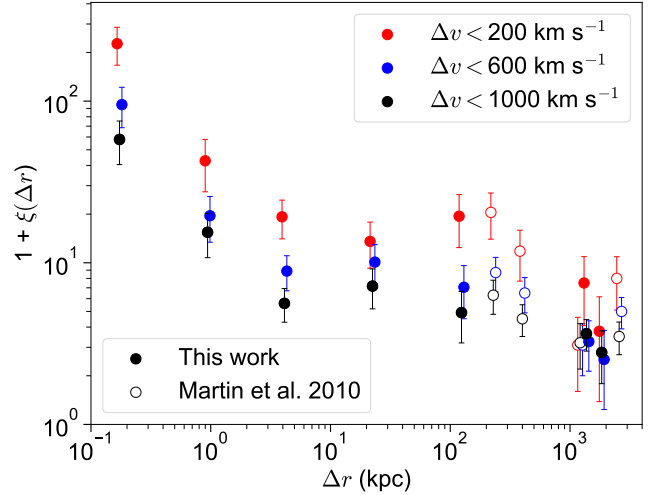


Fig. 5: Two-point correlation function ( $\xi(\Delta r)$ ) of CIV as a function of line-of-sight separation for 3 different bins of velocity. Red and blue points are slightly shifted for clarity from their identical position to the blue points. Open circle data points correspond to the measurements obtained by [Martin et al. \(2010\)](#).

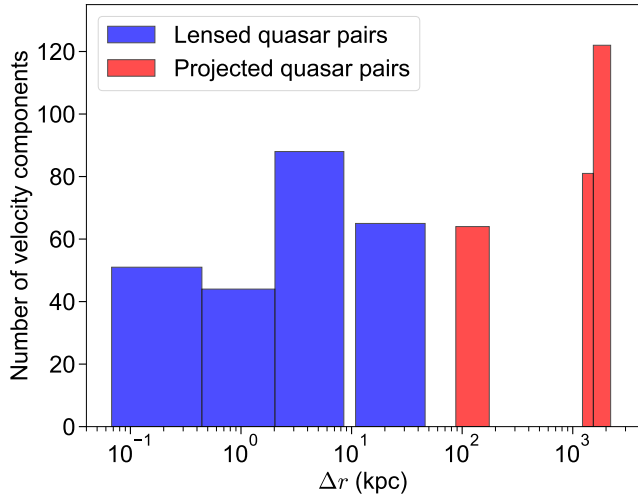


Fig. 4: Distribution of CIV velocity components. The blue histogram corresponds to velocity components found on lensed quasar pairs, while the red histogram corresponds to velocity components found on projected quasar pairs.

### 3.3. Transverse line-of-sight separations

For the projected pair case we computed  $\Delta r$  between lines-of-sight following [Hogg \(1999\)](#). For the lensed quasars, we calculated the separations by assuming the lens is produced by a point-like source, following [Krogager et al. \(2018\)](#):

$$\Delta r(z) = \begin{cases} \theta \frac{D_{AS} D_{OL}}{D_{LS}} & \text{Lensed quasars} \\ \theta \cdot D_{OA} & \text{Projected quasar pairs,} \end{cases} \quad (4)$$

where  $\theta$  is the angular separation on the sky of the quasar images; while the angular diameter distances are,  $D_{AS}$  from the

absorber to the quasar,  $D_{OL}$  from the observer to the lens,  $D_{LS}$  from the lens to the quasar, and  $D_{OA}$  from the observer to the absorber. The resulting range of  $\Delta r$  for the sample is  $20 \text{ pc} \lesssim \Delta r \lesssim 2.4 \text{ Mpc}$ . Fig. 4 shows the resulting distribution of  $\Delta r$ . The space between some bins is produced by gaps in the survey where no quasar pairs were found. We chose this binning to account for roughly a similar amount of velocity components in each bin without splitting the redshift path of a quasar line-of-sight. This binning is used throughout Section 4.

## 4. Transverse correlation analysis

### 4.1. Two-point correlation function

In order to study how CIV clusters at different scales, we defined the two-point correlation function,  $\xi(\Delta r, \Delta v)$ , as the probability excess, with respect to a randomly distributed sample, of finding a pair of velocity components with redshift  $z_A$  on lines-of-sight A and  $z_B$  on B having a velocity difference  $\Delta v = c|z_A - z_B|(1 + z_{AB})^{-1}$ , where  $z_{AB}$  is the average redshift, and a line-of-sight separation  $\Delta r$ . To compute  $\xi(\Delta r, \Delta v)$ , we followed similar implementations by [Martin et al. \(2010\)](#) and [Tejos et al. \(2014\)](#) of the generalized [Landy & Szalay \(1993\)](#) estimator, in our notation:

$$\xi(\Delta v, \Delta r) = \frac{D_A D_B / n_{DD} - D_A R_B / n_{DR} - D_B R_A / n_{DR}}{R_A R_B / n_{RR}} + 1, \quad (5)$$

where  $D_A D_B$  is the number of data-data pairs,  $R_A R_B$  the number of random-random pairs, and  $D_A R_B$  and  $D_B R_A$  are the data-random pairs. These pairs are computed by creating every possible combination of velocity components between line-of-sight A and B. The data-random pairs are built by pairing the data catalog from one line-of-sight with a random catalog generated with the other. These quantities are normalized by their respective normalization factors:

$$\begin{aligned} n_{DD} &= N_A N_B, \\ n_{DR} &= \alpha N_A N_B, \text{ and} \\ n_{RR} &= \alpha^2 N_A N_B; \end{aligned} \quad (6)$$

here,  $N_A$  and  $N_B$  are the total number of absorption lines found on lines-of-sight A and B respectively, and  $\alpha$  is a positive integer used to build the random catalogs, which we describe below. To create these pairs of velocity components, we only considered column densities above 90% completeness in line-of-sight B, with this same limit being applied on line-of-sight A. In total, this corresponds to 300 components in A, and 249 components in B ( $\approx 88\%$  of the total sample).

The creation of random catalogs is a delicate point when working with two-point correlation functions, as it largely depends on the geometry and type of objects involved. Here we followed the approach of [Tejos et al. \(2014\)](#) and created  $\alpha = 100$  copies of each measured parameter set ( $z, N$ ), by randomizing their redshifts. Each random redshift was drawn uniformly from any position on the quasar line-of-sight where the corresponding  $N$  could have been measured, depending on the spectral coverage and the column density limit given the signal-to-noise. This limiting column density was measured following Eq. 2. This way of randomizing the redshifts aids in reducing any sort of detection bias, as the spectra naturally have different S/N at different wavelengths.

The [Landy & Szalay \(1993\)](#) estimator is typically preferred because it minimizes the Poisson variance,  $(\Delta_{DD}^2(\xi) = (1 + \xi)/DD)$ . However, assuming only uncertainties due to Poisson variance, as discussed by [Mo et al. \(1992\)](#) and [Tejos et al. \(2014\)](#), may underpredict the real uncertainty. To remedy this potential issue, we adopted a more conservative approach by estimating our uncertainties ( $\Delta_{BS}^2$ ) via bootstrapping, computing our correlation measurements  $N_{BS} = 100$  times with a random sample (with repetition) of  $N_A$  velocity components on line-of-sight A, and  $N_B$  on line-of-sight B; then, for every bin:

$$\Delta_{BS}^2(\xi) = \frac{1}{N_{BS}} \sum_i^{N_{BS}} (\xi_i - \bar{\xi})^2, \quad (7)$$

where  $\bar{\xi}$  is the mean over all bootstrap measurements,  $\xi_i$ . Finally, to compute  $\xi$ , each type of pairs ( $D_A D_B, D_A R_B, D_B R_A, R_A R_B$ ) are summed up:

$$D_A D_B(\Delta v, \Delta r) = \sum_i^{N_{LOS}} D_A D_B(\Delta v, \Delta r)_i. \quad (8)$$

In Fig. 5 we show  $1 + \xi(\Delta r)$  binned for three values of maximum  $\Delta v$  as a function of  $\Delta r$ . The bins in separation are chosen so that each bin have roughly the same number of pairs when possible (same binning used in Fig. 4). The maximum  $\Delta v$  (200, 600, and 1000  $\text{km s}^{-1}$ ) were chosen to compare more directly with [Martin et al. \(2010\)](#) (open circles), where they analyzed data of 29 projected quasar pairs at medium spectral resolution; all of these pairs are different from the 12 found on our sample, making our results completely independent. The figure shows that the amplitude of  $\xi(\Delta r)$  generally increases with decreasing separation, although at scales between  $\approx 5$  kpc and  $\approx 500$  kpc,  $\xi$  seems to be constant across three bins when comparing with the smaller bin by [Martin et al. \(2010\)](#).

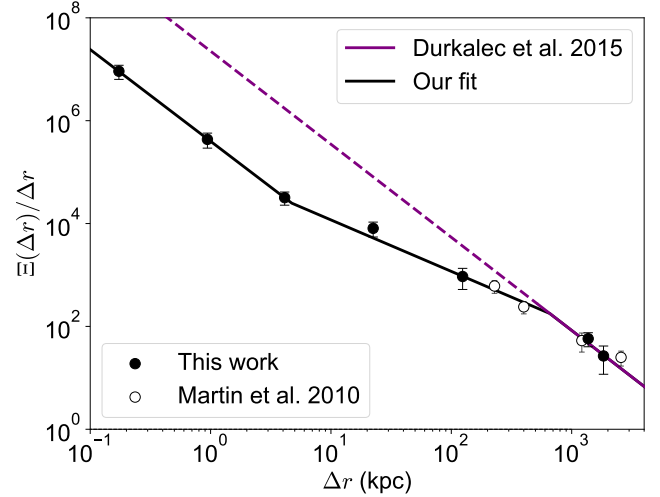


Fig. 6: Projected transverse correlation function ( $\Xi(\Delta r)$ ) for C IV. Open circle data points correspond to the measurements obtained by [Martin et al. \(2010\)](#). The bins are the same as the one from Fig. 5. The purple solid line shows a galaxy-galaxy auto-correlation function result ([Durkalec et al. 2015](#)), with parameters  $r_0 = 5.64^{+0.69}_{-0.77}$  Mpc and  $\gamma = 1.81^{+0.02}_{-0.06}$ , while the dashed purple line is its extrapolation to small scales. The solid black line corresponds to the model of Eq. 13, described further in the main text.

#### 4.2. Projected transverse correlations

In order to compare our measurements with galaxy autocorrelation studies and properly fit  $\xi(\Delta r)$ , we computed the "projected transverse correlation function" (PTCF) ([Davis & Peebles 1983](#)). The PTCF is the integral of  $\xi(\Delta v, \Delta r)$  over the distance in redshift space ( $\Delta \Pi$ ), which is obtained by assuming the observed  $\Delta v$  is produced by Hubble flow, therefore  $\Delta \Pi(\Delta v, z) = (1 + z)\Delta v/H(z)$ ; then, the PTCF is computed as,

$$\Xi(\Delta r, \Delta \Pi_{max}) = 2 \int_0^{\Delta \Pi_{max}} \xi(\Delta \Pi, \Delta r) d\Delta \Pi \quad (9)$$

Additionally, this can be approximated, given the cylindrical symmetry of the survey, following [Martin et al. \(2010\)](#) and [Tejos et al. \(2014\)](#), by:

$$\Xi(\Delta r, \Delta \Pi_{max}) \approx 2\Delta \Pi_{max} \xi(\Delta \Pi_{max}, \Delta r) \quad (10)$$

Also, [Davis & Peebles \(1983\)](#) showed that this function can be fitted using a power law of slope  $\gamma$  by assuming that the correlations in real-space take the form,  $\xi(\Delta r) = (r_0/\Delta r)^\gamma$ ; then:

$$\Xi(\Delta r) = A(r_0, \gamma) r^{1-\gamma}, \quad (11)$$

where  $A(r_0, \gamma) = r_0^\gamma \Gamma(1/2) \Gamma[(\gamma - 1)/2] / \Gamma(\gamma/2)$ , and  $\Gamma$  is the gamma function. It is important to note that this assumes a  $\gamma > 1$  and  $\Pi_{max} \rightarrow \infty$ . Then, a fit of  $\Xi(\Delta r)$  intermediately provides a value for  $r_0$  and  $\gamma$ .

In Fig. 6 we show  $\Xi(\Delta r)$  for the same velocity threshold bins as in Fig. 5. We chose the larger threshold, as the condition for Eq. 11 is that  $\Pi_{max} \rightarrow \infty$ . Open circles correspond to the measurements obtained by [Martin et al. \(2010\)](#), using the same velocity threshold and estimator, while the purple solid line shows

a galaxy-galaxy autocorrelation fit from Durkalec et al. (2015), extrapolated to lower separations with the purple dashed line.

We then fitted  $\Xi(\Delta r)$  in three different ways. First, we fitted a single power law (Eq. 11) with best-fit parameters  $r_0 = 4.63 \pm 1.18$  Mpc, and  $\gamma = 1.18 \pm 0.04$  (see Fig. C.1); while this fit works well at higher  $\Delta r$ , it underpredicts the smaller separation bin, and it does not consider the relation between C IV and galaxies. With this in mind, we consider the prediction from Scannapieco et al. (2006) that  $\xi$  should break and flatten somewhere at small separations.

Following Martin et al. (2010), we modify our fit to  $\Xi(\Delta r)$  to add a break to the power law of the form:

$$\xi(\Delta r) = \begin{cases} (r_0/r_1)^\gamma, & \Delta r < r_1 \\ (r_0/\Delta r)^\gamma, & \Delta r \geq r_1 \end{cases} \quad (12)$$

where the first regime delimited by  $r_1$ , is seen as a constant correlation  $\xi(\Delta r)$  (which when normalized is seen as  $\Xi(\Delta r)/\Delta r \propto 1/\Delta r$ ). Following Martin et al. (2010), we adopted the  $r_0$  and  $\gamma$  parameters from the galaxy autocorrelation function; this can be assumed if we consider that the correlation amplitudes of C IV and that of galaxies are the same at scales larger than the sizes of C IV enriched regions. We chose the result of Durkalec et al. (2015) with parameters  $r_0 = 5.64^{+0.69}_{-0.77}$  Mpc and  $\gamma = 1.81^{+0.02}_{-0.06}$ , as they study a sizable sample of 1556 galaxies at a similar redshift range  $2.0 < z < 2.9$ ; this way the only free parameter for this model is  $r_1$ , for which we find a best fit at  $r_1 = 597 \pm 130$  kpc, when considering the points from Martin et al. (2010) (see Fig. C.2). However, the flat  $\xi(\Delta r)$  prediction still shows an even larger offset at small  $\Delta r$  when compared with the single power law model; this is also noticeable in the increasing correlations at the very small scales ( $\Delta r < 10$  kpc) best seen in Fig. 5.

Taking this into consideration, we modified Eq. 12, to add a second break on  $\xi(\Delta r)$  to account for a third regime at the smallest separations:

$$\xi(\Delta r) = \begin{cases} (r_3/\Delta r)^{\gamma_1}, & \Delta r \leq r_2 \\ (r_0/r_1)^\gamma, & r_2 < \Delta r < r_1 \\ (r_0/\Delta r)^\gamma, & \Delta r \geq r_1 \end{cases} \quad (13)$$

where  $r_2$  and  $\gamma_1$  are the new free parameters, as  $r_3$  can be determined by imposing the continuity of  $\xi(\Delta r)$ , this way  $r_3 = r_2(r_0/r_1)^{\gamma/\gamma_1}$ . In Fig. 6 we present the resulting best fit for this model as the black line, corresponding to the best fit parameters:  $r_1 = 654^{+100}_{-87}$  kpc,  $r_2 = 4.70^{+1.60}_{-1.19}$  kpc, and  $\gamma_1 = 1.78 \pm 0.10$ . We again used the galaxy-galaxy autocorrelation measurements of  $\gamma$  and  $r_0$  (Durkalec et al. 2015), and we considered the data points from Martin et al. (2010). If we follow the same reasoning from the arguments for the first break of  $\xi(\Delta r)$ , a second break implies that these smaller scales are probing a different structure than the one we see at larger separations. Indeed, this model fits the data much closer than the simpler models that struggle at the smaller scales, which strongly supports the idea that we are probing a different kind of environment at the smaller scales probed by this survey ( $\lesssim 10$  kpc).

## 5. Discussion

The connection between galaxies and C IV is well documented (e.g., Adelberger et al. 2005; Martin et al. 2010; Turner et al. 2014; Bird et al. 2016; Rudie et al. 2019; Galbiati et al. 2023; Banerjee et al. 2023). For this reason, our fits from Eq. 12 and

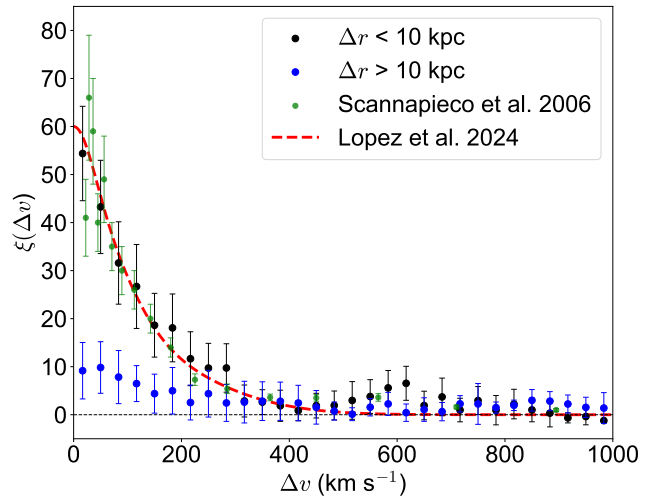


Fig. 7: Two-point correlation function ( $\xi(\Delta v)$ ) of C IV as a function of velocity across the two lines of sight for two different bins in separation, as the black and blue points for  $\Delta r < 10$  kpc and  $\Delta r > 10$  kpc respectively. The green points correspond to the single line-of-sight measurements obtained by Scannapieco et al. (2006). The red dashed line shows a prediction from transverse correlations of C IV using gravitational arcs (Lopez et al. 2024), adjusted to account for the different spectral and spatial resolution.

13 directly take into account the same correlation length from galaxies. In fact, our correlation measurements at the higher separation bins lie exactly on top of the galaxy autocorrelations (Fig. 6), also found by Martin et al. (2010) when comparing with Adelberger et al. (2005). This then suggests that C IV may be a good tracer of the way in which galaxies cluster at cosmic noon. However, we observe that the strong relation with galaxies does not hold at  $\Delta r \lesssim 500$  kpc, as seen in the flattening in of  $\xi(\Delta r)$  in Fig. 5 (this is the scale of the intermediate regime in Fig. 6, where  $\Xi(\Delta r)/\Delta r \propto 1/\Delta r$ ). It has been argued (Scannapieco et al. 2006; Martin et al. 2010; Mintz et al. 2022) that such flattening of  $\xi$  provides constraints on the sizes of C IV enriched regions around galaxies. The argument is based on the fact that, by decreasing  $\Delta r$ , we are not finding a significant number of additional pairs of velocity components, then implying that we are probing distances smaller than these regions. In conclusion, the break that we find on large scales with both models from Eq. 12, and 13 ( $597 \pm 130$  kpc and  $654^{+100}_{-87}$  kpc) is in good agreement with Martin et al. (2010) result of  $r_1 = 600 \pm 214$  kpc.

On the other hand, at the smaller scales probed here, Fig 5 shows that  $\xi(\Delta r)$  increases again. We attribute this to the fact that at this scale the autocorrelation is dominated by pairs of velocity components on the same absorption system. Therefore, this second break at  $r_2 = 4.70^{+1.60}_{-1.19}$  kpc would provide limits on the sizes of individual C IV clouds within the CGM of galaxies, instead of whole absorption systems. Unfortunately, the "sizes" of these clouds are difficult to constrain; for instance, Rauch et al. (2001) measure characteristic sizes of C IV clouds in the range  $r_0 = [3, 19]$  kpc, also using lensed quasars but a different method to constrain sizes. On the other hand, Lopez et al. (2024) find rather smaller sizes ( $\lesssim 1$  kpc) from kinematic arguments but concentrating on the very strong C IV systems towards gravitational arcs. The existence of a break in  $\xi$  at  $r_2 = 4.70^{+1.60}_{-1.19}$  kpc, as shown

in this work, strongly support the idea of a coherence length of the cool-warm CGM at the scale of a few kpc.

It is worth comparing with other species. Also using gravitational arcs [Afruni et al. \(2023\)](#) measured a coherence length of  $4.2^{+3.6}_{-2.8}$  kpc by studying absorption systems of Mg II at lower redshifts ( $z \sim 1$ ). Interestingly, this result is well within  $1\sigma$  from ours, even when considering the fact that C<sub>IV</sub> is more ionized and typically covers a larger cross section than Mg II (e.g., [Dutta et al. 2021](#)). Independently, [Rubin et al. \(2018\)](#) measured a coherence length lower limit of 1.9 kpc, which is still consistent with our result, but could also point towards a possible difference between the coherence length of these ions. Therefore, further work is needed to assess a possible difference between these coherence scales.

It is also interesting to make a comparison with independent measurements of clustering of C<sub>IV</sub> systems. To do so, we first projected  $\xi(\Delta v, \Delta r)$  in velocity. Fig. 7 shows  $\xi(\Delta v)$  in two bins around  $\Delta r = 10$  kpc. Notably, the amplitudes of  $\xi(\Delta v)$  in the two bins are quite different, which is expected given the results of Section 4; however, such difference makes a direct comparison with single quasar line-of-sight results more difficult. At small separations,  $\xi(\Delta v)$  becomes comparable with the velocity clustering measured directly towards single quasar lines-of-sight (green points), obtained using data with similar resolution at  $z \sim 2.2$  ([Scappapietra et al. 2006](#)). Based on this similarity, we fit our  $\xi(\Delta v)$  points at  $\Delta r < 10$  kpc using two Gaussians, following [Boksenberg & Sargent \(2015\)](#):

$$\xi(\Delta v) = A_1 \exp\left(-\frac{\Delta v^2}{2\sigma_1^2}\right) + A_2 \exp\left(-\frac{\Delta v^2}{2\sigma_2^2}\right), \quad (14)$$

where  $A_{1,2}$  are the amplitudes, and  $\sigma_{1,2}$  the corresponding standard deviations. We obtain a best fit with  $A_1 = 26.2 \pm 15.3$ ,  $\sigma_1 = 48.8 \pm 33$  km s<sup>-1</sup>,  $A_2 = 29.5 \pm 11.7$ , and  $\sigma_2 = 166.3 \pm 28.4$  km s<sup>-1</sup>. These standard deviations are consistent with the ones obtained by [Boksenberg & Sargent \(2015\)](#), at  $\sigma_{1,2} = 35.5, 105$  km s<sup>-1</sup>, suggesting that  $\xi(\Delta v)$  as measured by quasar pairs at small separations, where absorption profiles become more similar, is comparable to that measured using single lines-of-sight.

In an independent comparison, the red-dashed line of Fig. 7 shows the measurement obtained by [Lopez et al. \(2024\)](#). These authors computed a transverse  $\xi(\Delta v)$  for C<sub>IV</sub> absorption systems using a different technique, namely integral field spectroscopy of giant gravitational arcs, over separations of  $\Delta r \lesssim 10$  kpc. If we use the relation between  $\sigma$  of  $\xi$  for arcs and QSOs proposed by these authors, namely,  $\sigma_{\text{arc}} = \sigma_{\text{QSO}} / \sqrt{N}$ , where  $N$  is the mean number of clouds per spatial resolution element in [Lopez et al. \(2024\)](#), we obtain the relation shown by the dashed red line. This relation matches our measurements at  $\Delta r < 10$  kpc remarkably well considering the different methods. We conclude that measurements of  $\xi$  towards point-like and extended sources are indeed consistent with each other.

## 6. Summary

We have put together a sample of high-resolution spectra of 12 quasar pairs, to study the clustering of C<sub>IV</sub> absorption systems around cosmic noon. Our results are:

1. We detected 141 C<sub>IV</sub> absorption systems at  $z \sim 2$ , in parallel quasar line-of-sights (A & B) spanning separations between 20 pc and up to 2.37 Mpc.

2. We fitted Voigt profiles to all velocity components, resulting in a sample of 327 C<sub>IV</sub> velocity components on lines-of-sight A, and 293 on lines-of-sight B, with a column density distribution that is in good agreement with the known C<sub>IV</sub> statistics (Fig. 3).
3. We computed the two-point correlation function of C<sub>IV</sub> velocity components ( $\xi(\Delta v, \Delta r)$ ), using the [Landy & Szalay \(1993\)](#) estimator (Fig. 5). We find that the amplitude of  $\xi(\Delta r)$  flattens in the  $\sim 10 - 500$  kpc range, confirming previous predictions of flattening for the  $\xi(\Delta r)$  in this range ([Martin et al. 2010; Mintz et al. 2022](#)).
4. We computed the projected transverse correlation function ( $\Xi(\Delta r)$ ) (Fig. 6). We then used two models of  $\Xi(\Delta r)$  to estimate the coherence length of C<sub>IV</sub> absorption systems, for which we find best fits of  $597 \pm 130$  kpc and  $654^{+100}_{-87}$  kpc for the scale of these metal enriched regions.
5. For the smaller scales ( $\lesssim 10$  kpc) the correlation amplitude increases with decreasing separation. This suggests a different regime of the correlation function at scales  $r_2 < 4.70^{+1.6}_{-1.19}$  kpc, which we interpret as a relevant scale for the coherence length of C<sub>IV</sub> clouds.
6. Our results offer the first comprehensive picture of how metal-enriched regions cluster and are separately compatible with observations of C<sub>IV</sub> towards giant gravitational arcs (Fig. 7), and previous measurements of cloud sizes for C<sub>IV</sub> and coherence length of the CGM.

While our results suggest small coherence length of C<sub>IV</sub> clouds, further work is necessary to measure more precise correlation amplitudes at separations  $\lesssim 1$  kpc. To achieve this, more spectroscopic data on lensed quasars (or galaxies) are needed. On larger scales, additional data on quasars pairs would significantly aid to constrain the scale of the metal-enriched regions, which uncertainties are still of the order of the hundreds of kiloparsecs.

*Acknowledgements.* We would like to thank the anonymous referee for their constructive feedback and comments. H. C., S. L. and N. T. acknowledge the support by FONDECYT grant 1231187. P. A. acknowledges support from ANID-Subdirección de Capital Humano/Doctorado Nacional/2022-21222110.

## References

Adelberger, K. L., Shapley, A. E., Steidel, C. C., et al. 2005, ApJ, 629, 636  
 Afruni, A., Lopez, S., Anshul, P., et al. 2023, A&A, 680, A112  
 Banerjee, E., Muzahid, S., Schaye, J., Johnson, S. D., & Cantalupo, S. 2023, MNRAS, 524, 5148  
 Bird, S., Rubin, K. H. R., Suresh, J., & Hernquist, L. 2016, MNRAS, 462, 307  
 Boksenberg, A. & Sargent, W. L. W. 2015, ApJS, 218, 7  
 Bolmer, J., Greiner, J., Krühler, T., et al. 2018, A&A, 609, A62  
 Bordoloi, R., O'Meara, J. M., Sharon, K., et al. 2022, Nature, 606, 59  
 Bordoloi, R., Wagner, A. Y., Heckman, T. M., & Norman, C. A. 2017, ApJ, 848, 122  
 Chen, H.-W., Gauthier, J.-R., Sharon, K., et al. 2014, MNRAS, 438, 1435  
 Chen, Y., Steidel, C. C., Hummels, C. B., et al. 2020, MNRAS, 499, 1721  
 Churchill, C. W., Evans, J. L., Stemock, B., et al. 2020, ApJ, 904, 28  
 Cooke, J., & O'Meara, J. M. 2015, ApJ, 812, L27  
 Cooksey, K. L., Kao, M. M., Simcoe, R. A., O'Meara, J. M., & Prochaska, J. X. 2013, ApJ, 763, 37  
 Coppolani, F., Petitjean, P., Stoehr, F., et al. 2006, MNRAS, 370, 1804  
 Cristiani, S., Cupani, G., Trost, A., et al. 2024, MNRAS, 528, 6845  
 Davis, M. & Peebles, P. J. E. 1983, ApJ, 267, 465  
 D'Odorico, V., Calura, F., Cristiani, S., & Viel, M. 2010, MNRAS, 401, 2715  
 D'Odorico, V., Cupani, G., Cristiani, S., et al. 2013, MNRAS, 435, 1198  
 D'Odorico, V., Viel, M., Saitta, F., et al. 2006, MNRAS, 372, 1333  
 Durkalec, A., Le Fèvre, O., Pollo, A., et al. 2015, A&A, 583, A128  
 Dutta, R., Acebron, A., Fumagalli, M., et al. 2024, MNRAS, 528, 1895  
 Dutta, R., Fumagalli, M., Fossati, M., et al. 2021, MNRAS, 508, 4573  
 Faucher-Giguère, C.-A. & Kereš, D. 2011, MNRAS, 412, L118  
 Faucher-Giguère, C.-A. & Oh, S. P. 2023, ARA&A, 61, 131  
 Fernandez-Figueroa, A., Lopez, S., Tejos, N., et al. 2022, MNRAS, 517, 2214

Galbiati, M., Fumagalli, M., Fossati, M., et al. 2023, MNRAS, 524, 3474

Hasan, F., Churchill, C. W., Stemock, B., et al. 2020, ApJ, 904, 44

Hennawi, J. F., Strauss, M. A., Oguri, M., et al. 2006, AJ, 131, 1

Hogg, D. W. 1999, arXiv e-prints, astro

Kereš, D., Katz, N., Weinberg, D. H., & Davé, R. 2005, MNRAS, 363, 2

Kim, T. S., Partl, A. M., Carswell, R. F., & Müller, V. 2013, A&A, 552, A77

Krogager, J.-K. 2018, arXiv e-prints, arXiv:1803.01187

Krogager, J. K., De Cia, A., Heintz, K. E., et al. 2024, MNRAS, 535, 561

Krogager, J. K., Noterdaeme, P., O'Meara, J. M., et al. 2018, A&A, 619, A142

Landy, S. D. & Szalay, A. S. 1993, ApJ, 412, 64

Lehner, N., Wotta, C. B., Howk, J. C., et al. 2018, ApJ, 866, 33

Lopez, S., Afruni, A., Zamora, D., et al. 2024, A&A, 691, A356

Lopez, S., Ellison, S., D'Odorico, S., & Kim, T. S. 2007, A&A, 469, 61

Lopez, S., Reimers, D., Gregg, M. D., et al. 2005, ApJ, 626, 767

Lopez, S., Reimers, D., Rauch, M., Sargent, W. L. W., & Smette, A. 1999, ApJ, 513, 598

Lopez, S., Tejos, N., Barrientos, L. F., et al. 2020, MNRAS, 491, 4442

Lopez, S., Tejos, N., Ledoux, C., et al. 2018, Nature, 554, 493

Maitra, S., Srianand, R., Petitjean, P., et al. 2019, MNRAS, 490, 3633

Martin, C. L., Scannapieco, E., Ellison, S. L., et al. 2010, ApJ, 721, 174

Mintz, A., Rafelski, M., Jorgenson, R. A., et al. 2022, AJ, 164, 51

Mo, H. J., Jing, Y. P., & Boerner, G. 1992, ApJ, 392, 452

Mortensen, K., Keerthi Vasan, G. C., Jones, T., et al. 2021, ApJ, 914, 92

Murphy, M. T., Kacprzak, G. G., Savorgnan, G. A. D., & Carswell, R. F. 2019, MNRAS, 482, 3458

Nelson, D., Genel, S., Pillepich, A., et al. 2016, MNRAS, 460, 2881

O'Meara, J. M., Lehner, N., Howk, J. C., et al. 2017, AJ, 154, 114

O'Meara, J. M., Lehner, N., Howk, J. C., et al. 2015, AJ, 150, 111

Oppenheimer, B. D. & Davé, R. 2006, MNRAS, 373, 1265

Péroux, C. & Howk, J. C. 2020, ARA&A, 58, 363

Prochaska, J. X., Tejos, N., Crighton, N., et al. 2016, linetools/linetools: Second major release

Prochaska, J. X., Prochaska, J. X., & Burles, S. M. 2006, ApJ, 639, 766

Rauch, M., Sargent, W. L. W., & Barlow, T. A. 1999, ApJ, 515, 500

Rauch, M., Sargent, W. L. W., & Barlow, T. A. 2001, ApJ, 554, 823

Rubin, K. H. R., Diamond-Stanic, A. M., Coil, A. L., Crighton, N. H. M., & Stewart, K. R. 2018, ApJ, 868, 142

Rubin, K. H. R., Prochaska, J. X., Koo, D. C., et al. 2014, ApJ, 794, 156

Rudie, G. C., Steidel, C. C., Pettini, M., et al. 2019, ApJ, 885, 61

Saccardi, A., Vergani, S. D., De Cia, A., et al. 2023, A&A, 671, A84

Savage, B. D. & Sembach, K. R. 1991, ApJ, 379, 245

Scannapieco, E., Pichon, C., Aracil, B., et al. 2006, MNRAS, 365, 615

Schaye, J., Aguirre, A., Kim, T.-S., et al. 2003, ApJ, 596, 768

Songaila, A. 2005, AJ, 130, 1996

Steidel, C. C., Erb, D. K., Shapley, A. E., et al. 2010, ApJ, 717, 289

Taylor, M. B. 2020, in Astronomical Society of the Pacific Conference Series, Vol. 522, Astronomical Data Analysis Software and Systems XXVII, ed. P. Ballester, J. Ibsen, M. Solar, & K. Shortridge, 67

Tejos, N., López, S., Ledoux, C., et al. 2021, MNRAS, 507, 663

Tejos, N., Lopez, S., Prochaska, J. X., et al. 2009, ApJ, 706, 1309

Tejos, N., Lopez, S., Prochaska, J. X., Chen, H.-W., & Dessauges-Zavadsky, M. 2007, ApJ, 671, 622

Tejos, N., Morris, S. L., Finn, C. W., et al. 2014, MNRAS, 437, 2017

Tumlinson, J., Peebles, M. S., & Werk, J. K. 2017, ARA&A, 55, 389

Turner, M. L., Schaye, J., Steidel, C. C., Rudie, G. C., & Strom, A. L. 2014, MNRAS, 445, 794

Urbano Stawinski, S. M., Rubin, K. H. R., Prochaska, J. X., et al. 2023, ApJ, 951, 135

Vergani, S. D., Petitjean, P., Ledoux, C., et al. 2009, A&A, 503, 771

Welsh, L., D'Odorico, V., Fontanot, F., et al. 2025, A&A, 703, A274

Zafar, T., Péroux, C., Popping, A., et al. 2013, A&A, 556, A141

Zahedy, F. S., Chen, H.-W., Rauch, M., Wilson, M. L., & Zabludoff, A. 2016, MNRAS, 458, 2423

## Appendix A: Integral Constraint

A well known bias in correlation measurements that we did not address in the main text is the so-called "integral constraint". This comes from the fact that the redshift space of each quasar is limited. Then, when we measure positive correlation, this can cause a negative one somewhere else, but at the same time the real correlation can be assumed to be positive. As shown by [Landy & Szalay \(1993\)](#), the real correlation ( $\xi^{\text{real}}$ ) is related to the measured one ( $\xi$ ) by:

$$1 + \xi = \frac{1 + \xi^{\text{real}}}{1 + \xi_V}, \quad (\text{A.1})$$

where  $\xi_V$  is the integral constraint computed as follows:

$$\xi_V = \int_V G(r) \xi^{\text{real}}(r) d^2V, \quad (\text{A.2})$$

with  $G(r) = R_A R_B / n_{RR}$ . As we do not know  $\xi^{\text{real}}$  a priori, we only made a small correction following [Tejos et al. \(2014\)](#),

$$\xi = (1 + \xi_V)(1 + \xi) - 1$$

$$\xi_V = \int_V G(r) \xi(r) d^2V, \quad (\text{A.3})$$

which is a small correction in this case ( $\lesssim 1\%$ ), smaller than our uncertainties. We nonetheless applied this correction.

## Appendix B: Continuity of the projected transverse correlation function.

Imposing the continuity of  $\Xi$ , at  $\Delta r = r_2$ , it is immediate that,

$$\Xi(\Delta r) = \begin{cases} A(r_3, \gamma) \left(\frac{r_1}{r_2}\right)^{\gamma/\gamma_1} \Delta r^{1-\gamma_1}, & \Delta r \leq r_2 \\ A(r_0, \gamma) r_1^{1-\gamma}, & r_2 < \Delta r < r_1 \\ A(r_0, \gamma) \Delta r^{1-\gamma}, & \Delta r \geq r_1, \end{cases} \quad (\text{B.1})$$

## Appendix C: Additional fits to the projected transverse correlation function.

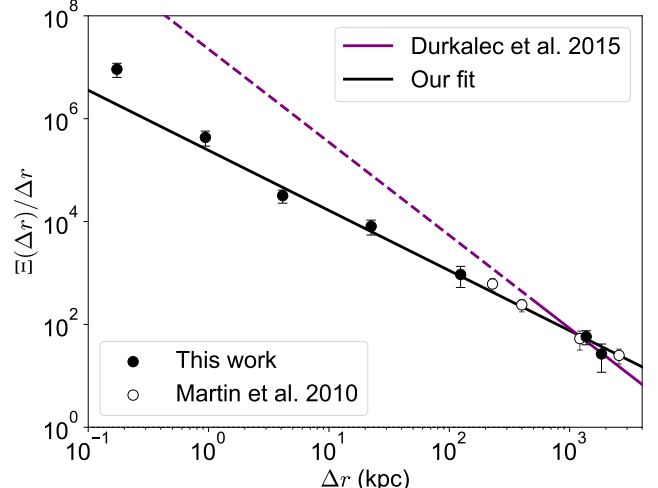


Fig. C.1: Projected transverse correlation function ( $\Xi(\Delta r)$ ) for CIV. Same as Fig. 6, with the difference that here we fit a single power law of the form shown in Eq. 11. Best fit parameters:  $r_0 = 4.45 \pm 0.56$  Mpc, and  $\gamma = 1.17 \pm 0.05$ .

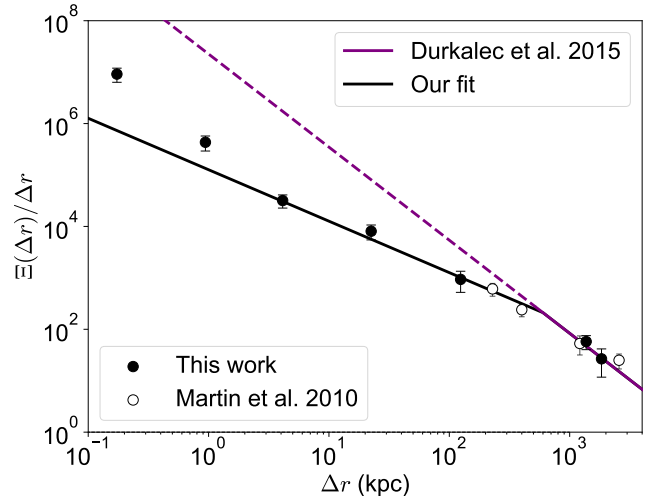


Fig. C.2: Projected transverse correlation function ( $\Xi(\Delta r)$ ) for CIV. Same as Fig. 6, with the difference that here we fit a broken power law of the form shown in Eq. 12. Best fit parameter:  $r_1 = 597 \pm 130$ .